On the closure of Collar's triangle by optical diagnostics

Saiz, Gabriel González; Sciacchitano, Andrea; Scarano, Fulvio

DOI
10.1007/s00348-022-03468-9

Publication date
2022

Document Version
Final published version

Published in
Experiments in Fluids

Experiments in Fluids (2022) 63:128
https://doi.org/10.1007/s00348-022-03468-9

RESEARCH ARTICLE

On the closure of Collar's triangle by optical diagnostics

Gabriel González Saiz[1] · **Andrea Sciacchitano**[1] · **Fulvio Scarano**[1]

Received: 22 October 2021 / Revised: 21 June 2022 / Accepted: 30 June 2022

Abstract

An experimental methodology is proposed to study aeroelastic systems with optical diagnostics. The approach locally evaluates the three physical mechanisms that produce the forces involved in Collar's triangle, namely aerodynamic, elastic, and inertial forces. Flow and object surface tracers are tracked by a volumetric particle image velocimetry (PIV) system based on four high-speed cameras and LED illumination. The images are analysed with Lagrangian particle tracking techniques, and the flow tracers and surface markers are separated based on the different properties of their images. The inertial and elastic forces are obtained solely analysing the motion and the deformation of the solid object, whereas the aerodynamic force distribution is obtained with pressure from PIV techniques. Experiments are conducted on a benchmark problem of fluid–structure interaction, featuring a flexible panel installed at the trailing edge of a cylinder. Data are collected in the resonant regime, where the panel exhibits a two-dimensional motion. The estimation of inertial and elastic forces is obtained enforcing a high-order polynomial fit to the surface motion and deformation. The aerodynamic loads on the panel are challenged by the need to devise adaptive boundary conditions complying with the panel motion. The closure of Collar's triangle yields overall residuals of about one-half of the inertial force taken as reference. The simultaneous measurement of the three forces paves the way to assessing the equilibrium of forces closing the Collar's triangle. The latter can be intended for uncertainty evaluation or, when only two forces are measured, for estimation of the remaining Collar element.

Graphical Abstract

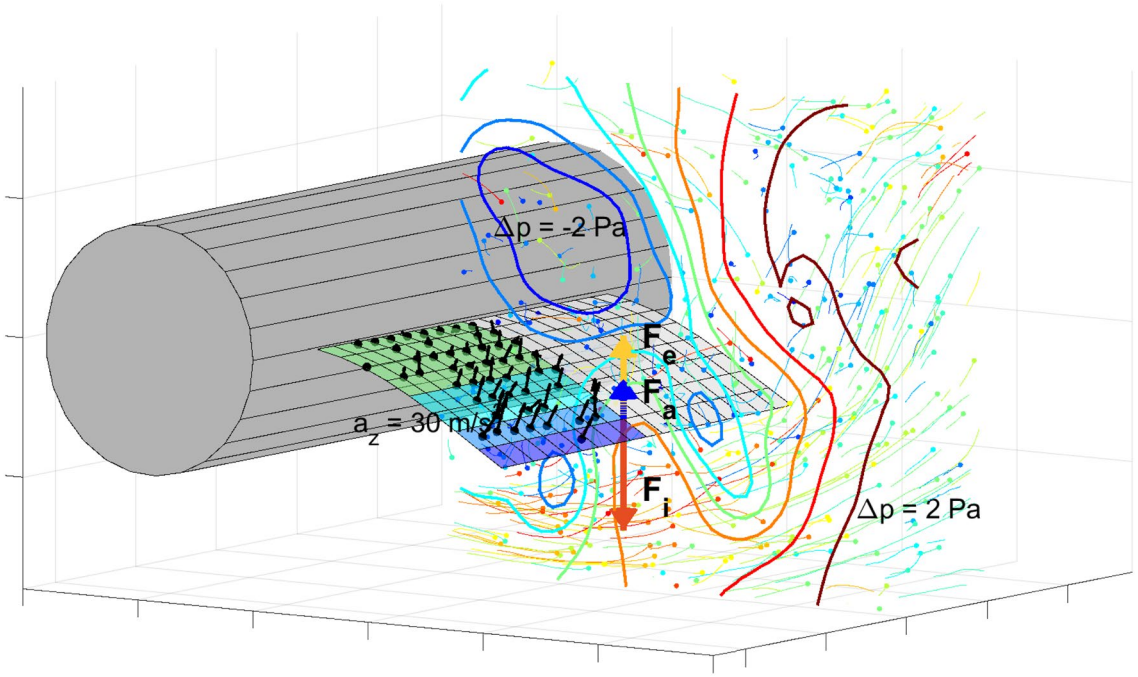

Extended author information available on the last page of the article

Published online: 08 August 2022

1 Introduction

Aeroelastic phenomena occur frequently in nature as well as in a wide number of engineering applications, most notably in civil (Sarkar et al. 1994), energy (Abdelkefi 2016) and power engineering (Marshall et al., 1996), and in the transport sector (Wright and Cooper 2008). In the aeroelastic regime, a flexible body immersed in a flow is subjected to the aeroelastic system of forces, namely aerodynamic, elastic, and inertial. Their mutual relationship was conceptualised in the so-called Collar's triangle (Collar 1947).

Still, nowadays, fluid–structure interaction (FSI) problems are difficult to study both with experimental as well as computational techniques. Computer simulations of the fluid flow coupled with a time-varying structural boundary remain a challenging task. Computational aeroelasticity reduces nowadays practical problems into simpler geometries (Schuster et al. 2003) for affordability. The numerical coupling of independent fluid and structural solvers, while improving the computational efficiency, poses new challenges at the fluid–structure interface, especially in the presence of structural or aerodynamic non-linearities, such as occurring in regimes with unsteady flow separation. This situation justifies the need to advance experimental approaches as a necessary tool for the validation of FSI simulations.

The first challenge encountered with FSI experiments is given by the problem of scaling. While Mach and Reynolds numbers are the most relevant parameters for aerodynamic scaling, FSI problems require consideration of the ratio of fluid and structure inertia alongside the structure relative stiffness (Friedmann 2004; Wan and Cesnik 2014).

Even when the problem is scaled to a satisfactory extent and the experiment is realised, monitoring the fluid flow and structure behaviour is hindered by the technical complexity of the needed instrumentation. Most of the works carrying out simultaneous measurements of flow and structure have been reported only in the last decade, and by combining optical techniques. Many studies have approached the flow measurements by planar particle image velocimetry; only a few have employed volumetric measurements (Kalmbach and Breuer 2013; Mitrotta et al. 2019). The measurement of the structure motions was performed either by digital image correlation (Bleischwitz et al. 2017; Marimon Giovannetti et al. 2017) or based on multiple-point laser triangulation (Kalmbach and Breuer 2013). Moreover, Timpe et al. (2013) directly measured the inertia forces on the structure with a force balance. Furthermore, Mitrotta et al. (2019) used the Lagrangian particle tracking technique (Schanz et al. 2016) to determine simultaneously the flow velocity and motion of the structure.

The combined use of PIV techniques (Adrian et al. 2011) and optical diagnostics like DIC or alike (DIC, Chu et al. 1985; ground vibration tests, Peeters et al. 2009; Image Pattern Correlation Technique or IPCT, Boden et al. 2014) to perform both tasks is a topic currently under development. Pressure from 3D-PIV enables the evaluation of the fluid flow pressure both in the fluid domain as well as in close proximity of the solid object surface (Liu and Katz 2006; van Oudheusden 2013). Pioneering work that applies pressure from PIV to FSI problems with generic three-dimensional and flexible structures has been conducted by Percin et al. (2017) for the case of a flexible membrane under mechanical actuation.

Finally, the evaluation of inertia forces, traditionally performed by means of accelerometers (as in-ground vibration tests, Peeters et al. 2009; or under in-flight conditions, Kehoe 1995), has also been surrogated by optical diagnostic methods. For example, the videogrammetric model deformation (VMD, Burner and Liu 2001) measurement technique captures the attitude of wings by tracking rows of markers on the model. Similarly, a new sensing approach (de Figueiredo et al. 2020) measures natural frequencies of aeronautical structures using a computer vision system. From the above, it can be stated that the use of optical techniques, such as PIV, offers the potential to provide a holistic analysis for FSI problems, compared to probe-based measurements.

Once it has been shown that aeroelastic forces can be measured by combining different optical techniques to study FSI phenomena, an element of novelty can be introduced: the principle of force equilibrium applied to Collar's triangle of aeroelasticity, formulated as the *Collar criterion*. The feasibility of invoking the Collar criterion to relate two or more elements of the Collar triangle is scrutinised in the present study. The potential benefit of such approach is to obtain a global evaluation of the experimental uncertainties when all forces are measured. Alternatively, when only two forces are accessed, the third one may be inferred using such equation.

The present work describes the foundational aspects of the experimental hardware and procedures needed to diagnose the aeroelastic forces non-intrusively by use of PIV techniques. The measurements are intended for the closure of Collar's triangle by a single experiment, that is, simultaneously determining all dynamic forces acting within the FSI problem. The demonstration makes use of a benchmark problem for aeroelasticity, i.e. the oscillation of a flexible thin plate trailing a circular cylinder immersed in a fluid stream.

2 FSI measurement working principle

Let us consider a flexible, thin panel of length L, width W and thickness T ($T << L, W$) in oscillatory motion induced by aerodynamic forces arising from the air flow as illustrated in Fig. 1. The aerodynamic loads consist of pressure p and

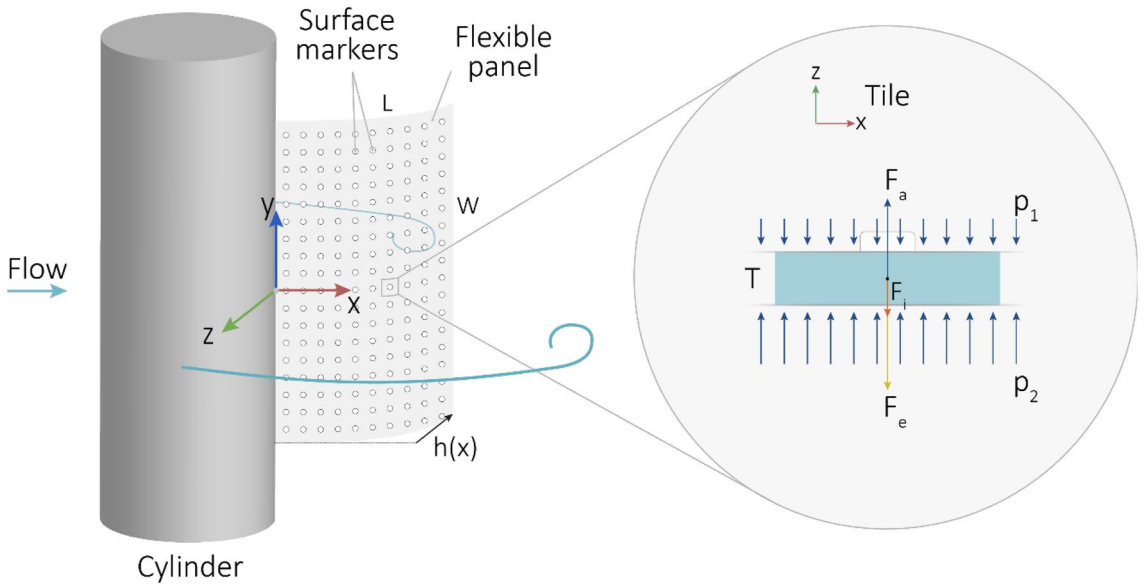

Fig. 1 Schematic of a cylinder-trailing foil system (left) and forces acting on a tile element (right). The coordinate system (streamwise, x; spanwise, y; transverse, z) chosen for the current work is included as reference

friction τ. The object opposes deformation by its stiffness, and acceleration motions by its inertia. Considering a square *tile* of such panel, i.e. a small element of side length l (see Fig. 1), the equilibrium of forces acting on such element reads as:

$$\sum \boldsymbol{F} = \boldsymbol{F}_{\mathrm{i}} + \boldsymbol{F}_{\mathrm{e}} + \boldsymbol{F}_{\mathrm{a}} = 0 \tag{1}$$

where $\boldsymbol{F}_{\mathrm{i}}$, $\boldsymbol{F}_{\mathrm{e}}$ and $\boldsymbol{F}_{\mathrm{a}}$ stand for the inertia, elastic, and aerodynamic forces, respectively. For the current work, the aforementioned vector identity will be reduced to the dominant direction of motion, z or transverse component, under the assumption of small deformations. As a consequence, the vector Eq. 1 is projected along z and rewritten as a scalar relation. Note that z will be used as coordinate along the thickness of the element, with $z=0$ corresponding to the middle of the plate in the undeformed state. In addition, for a simplified treatment of the problem, the quantities will be hypothesized uniform along the spanwise direction y; thus, the forces will be related solely to the streamwise component, x. The accuracy of the latter hypothesis is verified for the experiment presented in the remainder of the work.

2.1 Inertia force

A tile subject to non-zero elastic and aerodynamic forces will accelerate in proportion to such forces. Based on Newton third principle, the reaction force F_i due to inertia acts in the direction that opposes its acceleration a. For a tile element, the expression of the inertia force reads as:

$$F_i = -ma = -lwT\rho_m \cdot \frac{d^2h}{dt^2} \tag{2}$$

In the above equation, ρ_m is the density of the material, and the displacement of the plate mid-point along z is denoted by h, as illustrated in Fig. 1. The measurement of the object displacement and motion is typically performed by means of optical markers applied onto the surface of the panel. The markers' positions in time are recorded, while their velocities and accelerations are computed from time derivatives of the positions. The inertial force is then obtained by knowledge of the tile's specific mass and volume.

2.2 Elastic force

Elastic forces arise as a reaction of the object opposing deformation. The present discussion pertains to the linear elastic regime. For small displacements, the force can be considered to act normal to the surface and tensional forces (e.g. arising from aerodynamic skin friction) are neglected. In the above conditions, the whole elastic force reduces to the bending stress only.

Considering a thin deformable body, a 1-D simplification of the Kirchhoff–Love plate theory provides a relation between the deformation of the tile and the elastic forces, given its physical attributes. According to such theory, and invoking the strain–displacement and the stress–strain relations, the stress along the body reads:

$$\sigma_x = -\frac{E}{1-\nu^2} z \cdot \frac{\partial^2 h}{\partial x^2} \tag{3}$$

where E is the Young modulus, and ν is the Poisson ratio. The linear dependence on z indicates tensile/compressive stresses at the opposite faces of the panel. The non-uniform normal stress distribution gives rise to a moment reaction. Finally, considering the tile moment equilibrium, the elastic reaction force, which results normal to the surface, can be expressed as,

$$F_{\mathrm{e}} = -\frac{ElwT^3}{1-\nu^2} \cdot \frac{\partial^4 h}{\partial x^4} \tag{4}$$

The complete derivation of the Kirchhoff–Love plate theory for 3D solids can be found in the book of Panc (1975). Once the material properties are known, the experimental evaluation of the elastic force relies on the assessment of the 4th spatial derivative of the instantaneous deformed shape $h(x)$. The latter is regarded as a challenging task for an experiment, where even a small extent of measurement noise propagates and amplifies through the multiple operations of spatial differentiation.

2.3 Aerodynamics force

Aerodynamics loads are usually decomposed into normal (pressure) and shear (friction) stresses. Friction is negligible in most aeroelastic regimes (Fung 2008). Moreover, the pressure loads on a thin panel reduce the discussion to the pressure difference Δp from its opposite sides. The aerodynamic force acting on the tile reads as:

$$F_{\mathrm{a}} = \Delta p l w \tag{5}$$

The pressure field can be inferred from the velocity (and acceleration) distribution invoking the momentum equation. The latter in turn requires the numerical solution of the Poisson equation for pressure (van Oudheusden 2013). The instantaneous aerodynamic force is not straightforward to obtain from fluid flow measurements as it typically requires high-quality time-resolved 3D measurements (Beresh 2021). Moreover, the choice of boundary conditions can largely affect the evaluation of the pressure field (Neeteson et al. 2016). To minimize errors due to low spatial resolution or unwanted light reflections close to solid surfaces, the surface pressure is typically estimated imposing Dirichlet boundary conditions for the pressure values in the external flow region, where the Bernoulli relation between pressure and velocity holds true. In the rotational flow region (shear layers and separated wake), the integration of the pressure can follow the 3D propagation scheme recently proposed by Jux et al. (2020). It should be stressed that the evaluation of the unsteady pressure distribution over a generic surface, curved and in motion, time-resolved three-dimensional flow field measurements are required that surround such surface.

2.4 Collar's triangle of forces

Equation 1 can be rewritten combining the explicit terms obtained in Eqs. 2, 4 and 5. The resulting equilibrium of forces is expressed as:

$$-T\rho_m \cdot \frac{d^2 h}{dt^2} + \frac{ET^3}{1-\nu^2} \cdot \frac{\partial^4 h}{\partial x^4} + \Delta p = 0 \tag{6}$$

From such equation, the structural parameters (plate thickness T) and material properties (density ρ_m, Young modulus E, and Poisson ratio ν) need to be known. The corresponding values applying to the current experiment are gathered in Table 1. The remaining elements in the equation, such as the pressure difference Δp, the local acceleration and the spatial derivatives of the deformed shape need to be measured to close the problem.

It is worth mentioning that although the above identity theoretically holds, the experimental determination of such forces has inherent uncertainties. The latter is mostly associated with the measurement techniques adopted to monitor the flow and object motion. Therefore, one can already predict a residual force when computing the force equilibrium for Collar's triangle, referred to as Collar closure criterion (CC) force $\varepsilon_{\mathrm{CC}}$:

$$\varepsilon_{\mathrm{CC}} = -T\rho_m \cdot \frac{d^2 h}{dt^2} + \frac{ET^3}{1-\nu^2} \cdot \frac{\partial^4 h}{\partial x^4} + \Delta p \tag{7}$$

In the present study, an optical diagnostic system based on PIV techniques is developed for the purpose of determining the above forces. The fluid flow velocity is obtained over an extended three-dimensional domain by tracking large tracers (sub-millimetre helium-filled soap bubbles, HFSB, Scarano et al. 2015) along their trajectories to determine the flow pressure. The acceleration of the structural element is measured by tracking the motion of surface markers with the same algorithm as for the fluid tracers. Finally,

Table 1 Physical properties of the flexible foil and tile

Dimensions	Thickness, T (mm)	0.25
	Length, L (mm); l (mm) (tile)	95, 10
	Width, W (mm); $w = l$(mm) (tile)	200, 10
	Aspect ratio, L/W	0.475
Material	Density, ρ_m (kg/m^3)	1290
	Young modulus, E (GPa)	1.0
	Poisson ratio, ν (−)	0.3
Interaction parameters	Mass ratio, m* = (ρ_m/ρ_f).(T/L) (−)	2.77
	Cauchy number, Ca = ($\rho_f U^2$ W L^3)/EI (−)	7.8

the deformation of the panel is inferred from the analysis of the markers position and their relative displacement, respectively.

3 Experimental apparatus and procedure

3.1 Flow facility and model

The experiments were conducted at the Aerodynamics laboratory of TU Delft, in an open-jet open-return wind-tunnel of 600×600 mm^2 exit cross section. A cylinder of 90 mm diameter was installed vertically with a flexible transparent foil attached along the rear mid-plane. The foil (size 105×200mm^2) undergoes a 2D motion excited by the periodic shedding of vortices in the Karman wake of the cylinder. The maximum amplitude of oscillations in a 2D regime is observed at a free stream velocity $U_\infty = 2.25$m/s ($\mathrm{Re} = 1.35 \times 10^4$), where experiments are conducted. The foil optical transparency allowed to track flow tracers at both sides of it even when looking from only one side. However, the amount of detected flow tracers behind the foil was slightly lower than in the region with direct view, as a result of incomplete light transmission through the foil.

For the measurement of the foil kinematics, a regular pattern of 210 bright surface markers was applied to the foil. The markers had an average diameter $d_\mathrm{m} = 0.8$mm and a pitch $p_\mathrm{m} = 1$cm. The overall experimental setup is illustrated and provided in Fig. 2.

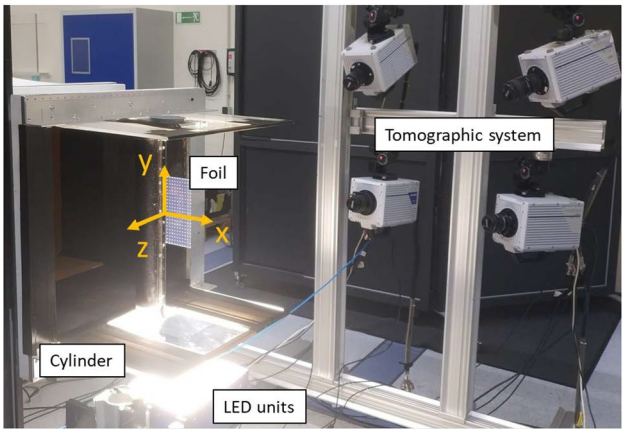

Fig. 2 Experimental arrangement with cylinder and foil and system of coordinates. Illumination (by LED units) and tomographic imaging system (four CMOS cameras). The system in action is illustrated by a video in Online Resource 1

3.2 Flow measurement

The flow was seeded with neutrally buoyant sub-millimetre (mean diameter $d \approx 350\mu$m) helium-filled soap bubbles (HFSB, Scarano et al. 2015), released by an in-house 200-generator seeding rake installed in the tunnel settling chamber (similarly to Jux et al. 2020). The nominal production rate of the flow tracers is 6×10^6 bubbles/s, resulting in a seeding concentration of ~ 10 bubbles/cm^3 for a free stream velocity $U_\infty = 2.25$m/s at the test section (seeded streamtube of 60×25cm^2). For the current experiment, only 100 generators were operated to reduce the seeding concentration to ~ 5 bubbles/cm^3, so as to satisfy the condition on the maximum number of particles per pixel ($ppp = 0.05$) for 4-camera tomographic systems (Elsinga et al. 2006; Scarano, 2013).

A measurement volume of $22 \times 40 \times 20$cm^3 was illuminated vertically (spanwise direction) by two *LaVision Flashlight 300* LED banks located under the test section. In the current experiments, flow tracers were measured at both sides of the transparent foil. A mirror was installed at the top plane of the test section to increase the light intensity in the measurement volume, thus allowing to identify the tracer particles also in the region behind the foil. The imaging system consisted of four high-speed cameras (1024×1024 pixels, 12 bit, 20 μm pixel pitch) mounted in a tomographic configuration 90 cm away from the foil, as shown in Fig. 2. The cameras subtended an aperture of approximately 30 degrees. Details of the optical system used in the experiments are summarized in Table 2.

The image acquisition and processing were conducted with the LaVision Davis 10.0.5 software. Sets of 5000 images were recorded in continuous mode at a rate of 1 kHz. Samples of the latter can be visualized in Fig. 3. For the calibration process, a geometrical calibration (Soloff et al.

Table 2 Optical system information

Tomographic system	
Illumination	2 × LaVision *Flashlight 300* LED
Cameras	2 × Photron *FastCam SA1.1* (1024 × 1024 pixels, 5400 fps)
	1 × Photron *FastCam SA5* (1024 × 1024 pixels, 7000 fps)
	1 × HighSpeedStar 8 (1024 × 1024 pixels, 7000 fps)
Imaging	3 × Objectives Nikkor 50 mm—f# 1/11.2
	1 × Objectives Nikkor 60 mm—f# 1/11.2
Acquisition frequency	1000 Hz

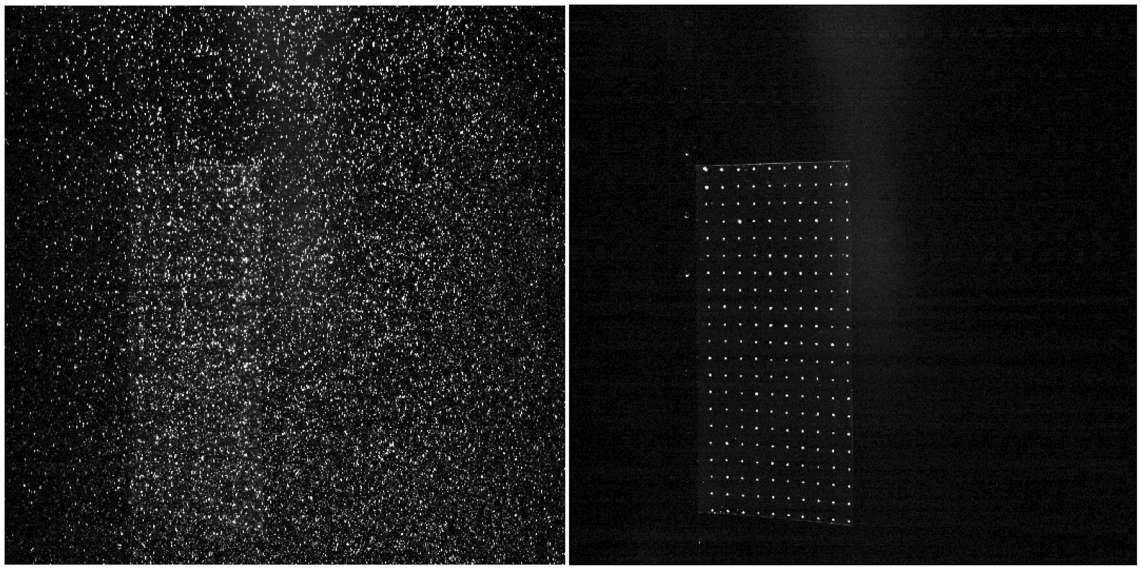

Fig. 3 Left: digital recording capturing the marked surface and HFSB flow tracers (see also animation in Online Resource 2). Right: digital recording of surface markers only (motion video in Online Resource 3)

1997) was followed by the volume self-calibration (Wieneke 2008) and optical transfer function determination (OTF calibration, Schanz et al. 2012). The surface markers were visually distinguished from the flow tracers based on their distinct optical characteristics. In order to track most fluid tracers (spherical bubbles) and most structural markers (2D flat bright circles), the volume self-calibration and the OTF calibration were performed separately with clean runs containing only one tracer type. Both the flow tracers' velocities and the foil markers motions were evaluated by means of the Shake-the-Box Lagrangian Particle Tracking (LPT) algorithm (Schanz et al. 2016). Based on the work of Battacharya and Vlachos (2020), particle location uncertainty is expected below 0.3 pixels for IPR-based reconstructions and further decreases to 0.1 pixels when the particles are track over multiple time instants with the STB algorithm (Sciacchitano et al. 2021).

4 Data reduction for load estimation

The following section describes the data reduction procedure to obtain the distribution of forces along the foil from the analysis of the tracers and markers motion.

4.1 Structural forces

As explained in Sect. 2, inertial and elastic forces are determined from the time and space derivatives, respectively, of the measured instantaneous foil's shape. In order to avoid noise propagation through the derivation process, a spatio-temporal least-square regression is performed on the locations of the markers to generate a coherent smooth surface. The regression makes use of a high-order polynomial in space (5th for x-direction and 2nd for y-direction) and a 2nd order in time, which is applied to all the measured markers over time stencil of 17 samples (~ 10% of one oscillation cycle). The resulting foil's shape is calculated on a Cartesian grid with 0.5 cm spacing in both streamwise and spanwise (x and y, respectively) directions. Therefore, the foil can be considered as discretised by adjacent square tiles, each centred at a grid node and having a surface area of 0.25 cm^2 (0.5 cm × 0.5 cm). The derivations in time and space to determine the acceleration and elastic force, respectively, are conducted analytically based on the polynomial description of the foil's instantaneous shape. The uncertainty of the elastic and inertia forces is quantified based on the uncertainty of the regression coefficients of the least-square fit (Montgomery et al. 2021) and linear error propagation.

The comparison between the raw markers' measurements and the foil's position and acceleration based on the regression analysis is illustrated in Figs. 4 and 5. Figure 4 compares the kinematics in time of a tracked surface marker with that of its projection onto the reconstructed surface. From this figure, the periodicity of the foil's motion both in terms of displacement and acceleration is evident, with the oscillation period equal to $T = 175$ ms. The use of the least-square regression allows to reconstruct missing time samples throughout the entire sequence (Fig. 4-left) and to clearly suppress the noise in the foil's acceleration (Fig. 4-right). Figure 5 displays the instantaneous location of the markers (in black circles) and the fitted surface at one of the

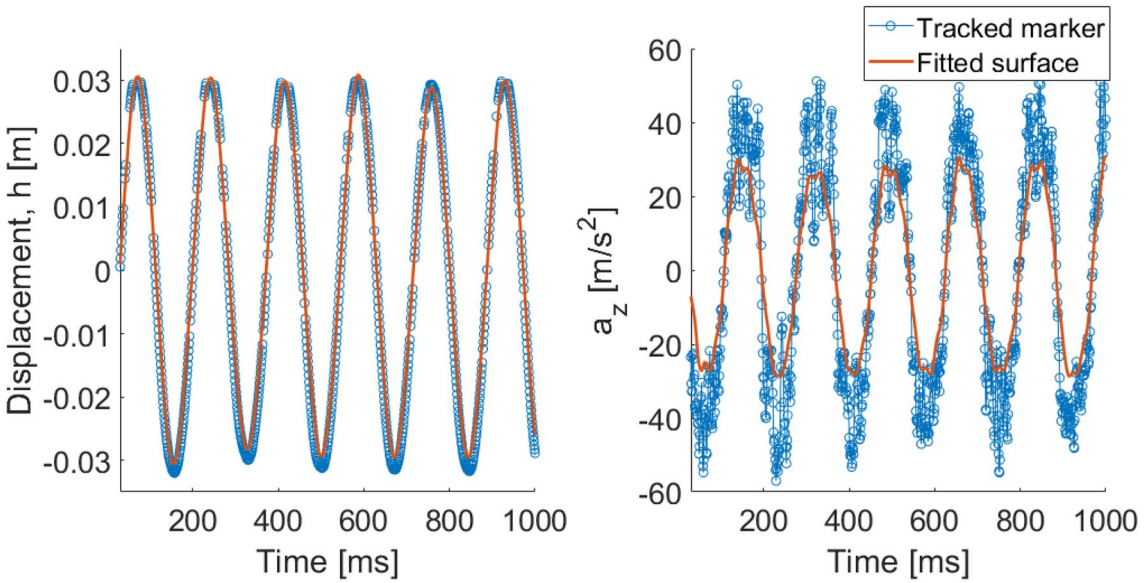

Fig. 4 Kinematics of a measured surface marker (dotted blue) and projection onto the fitted surface (solid red) at the location ($x/L=0.75$, $y/W=0.5$). Left: marker displacement; Right: marker acceleration

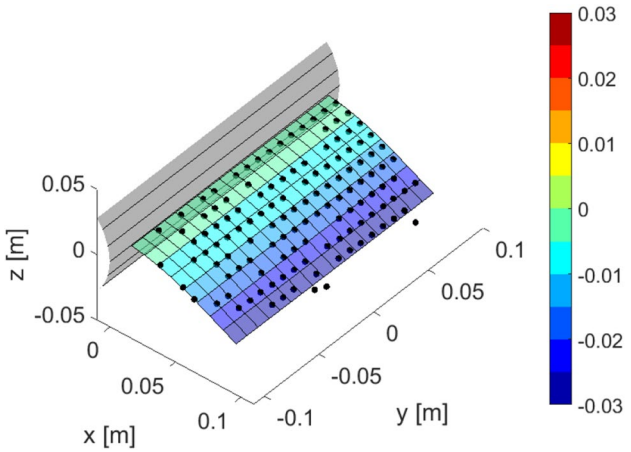

Fig. 5 Instantaneous description of raw markers (in black circles) with the fitted surface colour-coded by transverse displacement h (in [m]). Video of moving system is provided in Online Resource 4

extrema of the cycle, showing a contour of the transverse displacement. Even when some of the markers are not correctly reconstructed, the regression surface provides a full description of the entire foil.

4.2 Fluid load

Finally, the surface pressure distribution along the foil is evaluated for the determination of the aerodynamic forces. The volumetric pressure field is computed based on the solution of the Poisson equation for pressure in incompressible fluids (De Kat and van Oudheusden 2012), which results from the divergence of the equation of conservation of momentum:

$$\nabla^2 p = \nabla \cdot \left(-\rho_f \frac{D\overline{u}}{Dt} + \mu \nabla^2 \overline{u} \right) \tag{11}$$

The computation of the pressure field relies upon the material derivative of the velocity $D\overline{u}/Dt$, which is readily available from the LPT measurements, and the viscous dissipation $\mu\nabla^2\overline{u}$. Due to the high Reynolds ($\mathrm{Re} = 2 \times 10^4$), the latter term is neglected for the pressure computation. As shown by van Oudheusden et al. (2007) for a flow problem at similar Reynolds number, even in regions of high flow curvature, the viscous contribution to the pressure gradient is two orders of magnitude smaller than the other contributions.

Dense velocity reconstruction from particle tracks is performed with the *VIC#* algorithm implemented in DaVis 10.1 (Jeon et al. 2018). The approach is based on the Vortex-in-Cell method for VIC + (Schneiders and Scarano 2016) and optimises the vorticity field that best fits the measured velocity and acceleration by minimizing a cost function J built upon the disparity between the computed and the measured variables. Pressure integration is performed simultaneously to the velocity reconstruction by solving the Poisson equation with Neumann conditions at every boundary and a constant Dirichlet condition at a free stream location.

Because the applicability of the VIC# algorithm is limited to Cartesian domains not containing solid objects, the pressure reconstruction is only performed over two separate regions of the measurement domain that span from its

outmost boundaries to the limits of the foil motion (approximately 4 cm away from the neutral position of the foil). Hence, the foil does not enter the fluid domain under consideration for the VIC# reconstruction (black rectangles in Fig. 6). For the determination of the actual surface pressure on the foil, the pressure is then extrapolated towards the foil location (from both sides) via a nearest neighbour approach, neglecting the change of static pressure across the shear layer and the wake (Schlichting and Gersten 2016).

In order to determine an upper bound of the uncertainty of the reconstructed pressure, the aforementioned approach is performed from the outer regions towards the mid location ($z = 0$) at downstream locations of the trailing edge of the foil. The directions of extrapolation and the mid location are shown with black arrows and a red cross in Fig. 6, respectively. The difference in static pressure at the latter location when computing it from opposite directions, $\varepsilon_p = 1.7$ Pa, gives an estimation of the uncertainty of pressure jump across the foil.

5 Results

The flow velocity fields are analysed first, before discussing the loads of Collar's triangle and the resulting structural motion. Despite the 3D flow measurement, given the oscillations feature a quasi-2D behaviour and for sake of conciseness, only 2D flow data will be presented and discussed. The latter assumption is verified on both structural and flow data. The foil deformation presents a 2.5% deviation over different locations along the span of the foil. For the flow, the streamwise velocity component is taken as reference. The standard deviation along the span reaches at most 10% of the local average velocity, which is ascribed to the inherent turbulence of the flow. Hence, spanwise averaging is considered a valid approach in this problem to enhance the data density without any loss of flow or structural information.

A view in the median x–z plane illustrates velocity vectors and contours of the streamwise component (Fig. 7-top row). The values shown are averaged along the y-direction, where also the foil location is indicated. The velocity field reveals the oscillatory behaviour of the wake as expected in the regime of Kármán vortex shedding. The foil position also reveals its oscillatory motion. However, the foil does not appear to be in phase with the wake axis oscillations. The position and phase of the vortices shed in the cylinder wake are made more evident by displaying the transverse velocity component, where a negative blob followed by a positive one indicates a counter-clockwise rotating Kármán vortex. The dominant frequency of the flow could be already inferred from the sequence, and it corresponds to that of the flapping foil, $f \approx 5.7$Hz. The latter is verified from the time evolution of the transverse flow velocity, displayed in blue in Fig. 8. Note that the computed Δp is also included in Fig. 8 and exhibits a different frequency, in particular double to that of the transverse velocity. This can be explained from the fact that low-pressure regions arise at the vortex core locations regardless of the rotation direction of the vortex, thus resulting in double the pressure dominant frequency with respect to the flow. Nevertheless, the measured flow dominant frequency agrees well with the characteristic frequency for cylinder shedding wakes in the sub-critical regime, $St \approx 0.2$ (Williamson 1996), apparently, unaffected by the presence of the flexible foil.

Figure 7 (bottom row) illustrates a sequence of the pressure field time evolution. Recall that, due to the limitations of the available pressure solvers, an accurate pressure field could be calculated in the outer regions, i.e. away from the foil. Therefore, for the current visualization, the effect of the foil (imparting a small pressure discontinuity at its opposite faces) is neglected, and the pressure equation is solved in the entire measurement domain. Despite the expected errors at the vicinity of the solid interface, the pressure fields provide insights to the structure and phase of the aerodynamic forcing mechanism. The presence of low-pressure blobs,

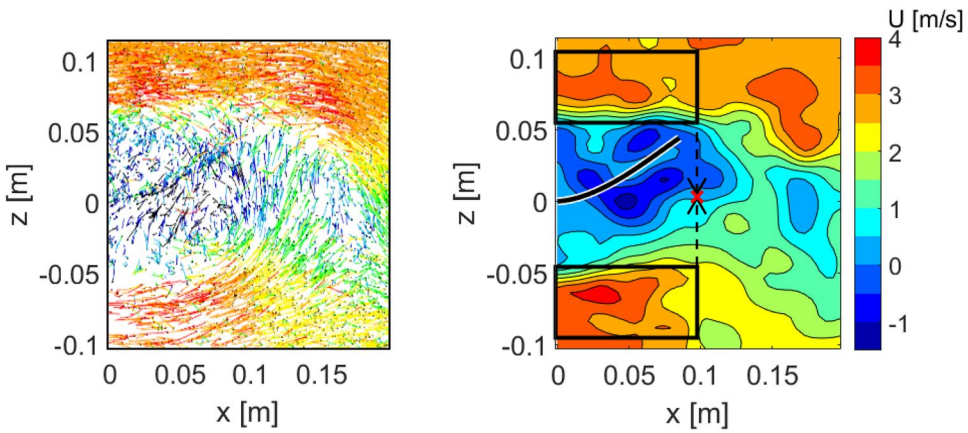

Fig. 6 Left: particle tracks in a slide of the measurement domain colour-coded by streamwise velocity. Right: instantaneous streamwise velocity reconstructed at the same time instant. Pressure evaluation in the regions highlighted by black rectangles

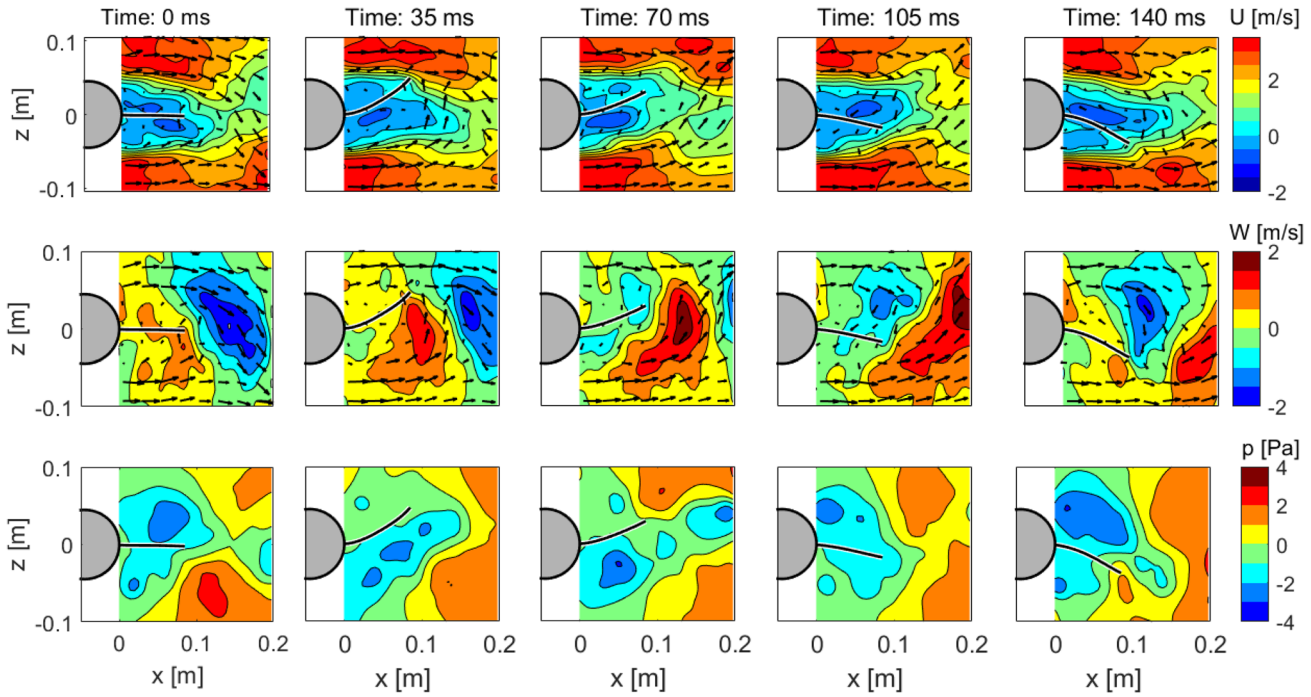

Fig. 7 Time sequence of flow velocity and pressure after spanwise averaging. Colour contours of streamwise (top) and transverse (middle) velocity component. Bottom row: static pressure field. Animation provided in Online Resource 5

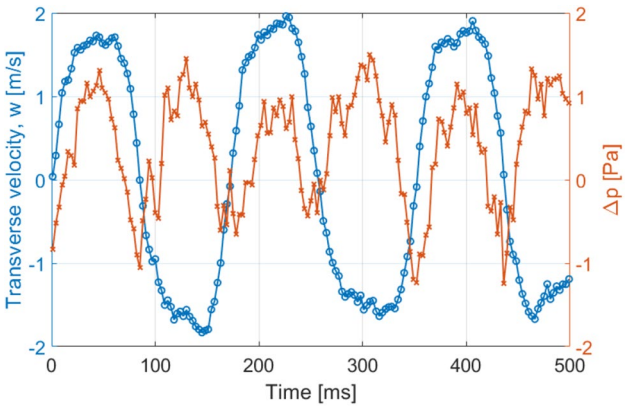

Fig. 8 Transverse flow velocity (blue, circles) and static pressure (red, crosses) at a location downstream of the foil, averaged along the span ($x/L = 1.1, z/L = 0$)

corresponding to the core of Kármán vortices, is observed, alternating from the opposite sides of the foil and travelling at the same convection speed of the vortices. During the passage of a low-pressure blob, the foil is accelerated in the direction of the vortex and continues after the vortex has passed the foil tip under the effect of inertia.

A time evolution of the computed surface pressure along the streamwise direction x is provided in Fig. 9. Note that as the foil deflects, the projection to the x-axis reduces the range to $0 < x/L < 0.9$ depending on the motion phase. Regarding the forcing, the most effective appears to occur when the low-pressure region transits from the foil mid-length ($x/L = 0.6$) to its end ($x/L = 0.9$). In this situation of maximum forcing, both the pressure load (a pulling force) and the foil velocity vector are aligned, thus resulting in a positive work performed by the flow to the foil. This mechanism is enhanced by the high-pressure regions (red orange in Fig. 7), which build up in the outer region when the foil is at the limit of the motion and aid to push the foil back towards the neutral position. The above effects ultimately lead to an oscillatory aeroelastic regime with pronounced periodic behaviour.

The time evolution of the foil's motion is illustrated in Fig. 10. Contours of position, tiles' acceleration, and elastic force per tile are provided on the deformed shape of the foil. Position (left column) and acceleration of the foil (centre column) are in phase-opposition, as expected from the second derivative of an oscillatory motion. The inertia force (not shown here) is opposite to the acceleration; hence, it exhibits the same trend as the foil's displacement. Similarly, to the acceleration, the elastic force opposes to the foil position, as the deformation promotes internal stresses and moments that act against it to recover the undeformed state. This working mechanism is analogous to that of a mass-spring system in oscillation.

Figure 11 illustrates the foil motion by the time evolution of three markers located at the mid-span of the foil and at 1/4, 1/2 and 3/4, respectively, of the foil's chord length.

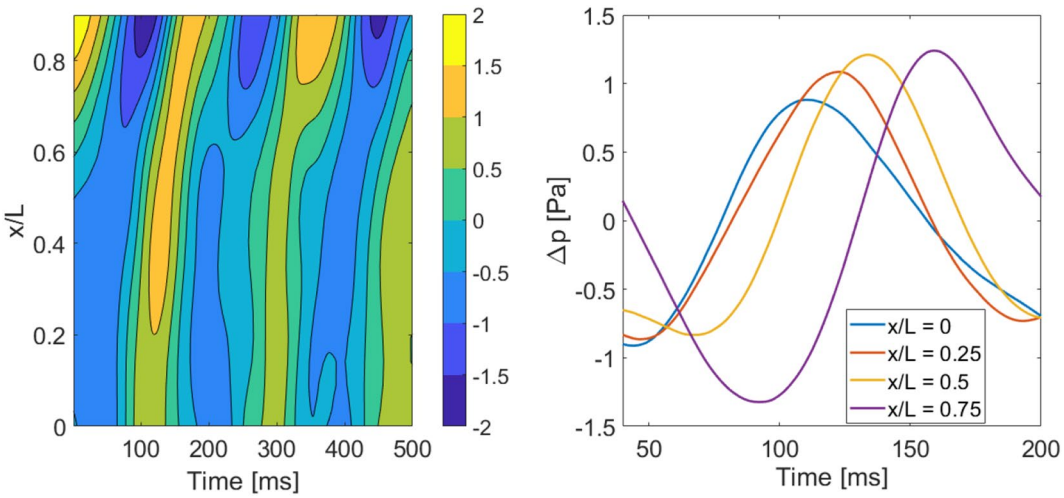

Fig. 9 Left: time evolution map of surface pressure (in Pascals) along the normalized streamwise direction x/L. Right: time evolution of surface pressure for extracted locations $x/L = 0, 0.25, 0.5, 0.75$

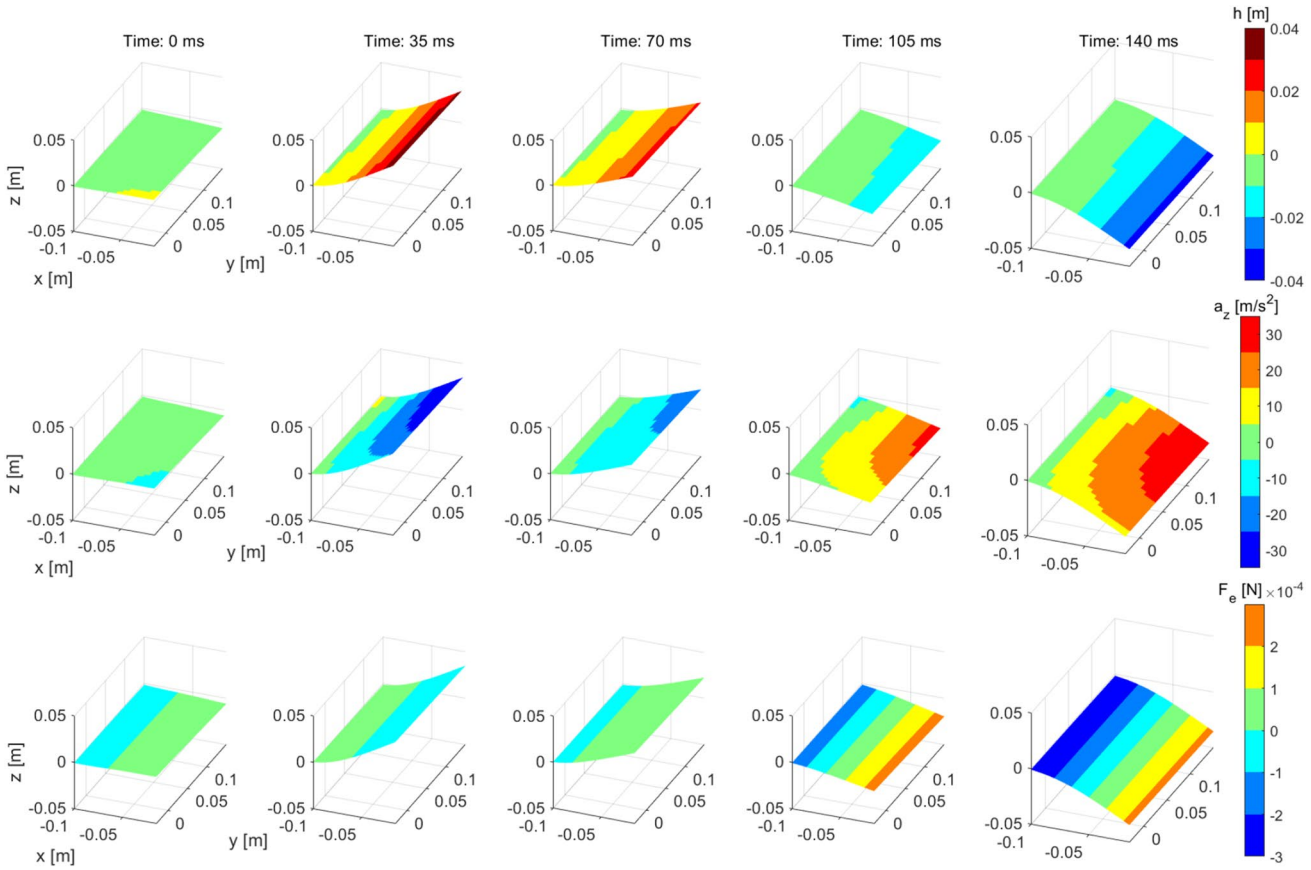

Fig. 10 Time sequence of measured structural variables: displacement h (top), tiles' acceleration (related to the inertia forces, centre), and elastic force along z (bottom) acting on a tile of 0.5×0.5 cm^2. Animation provided in Online Resource 6

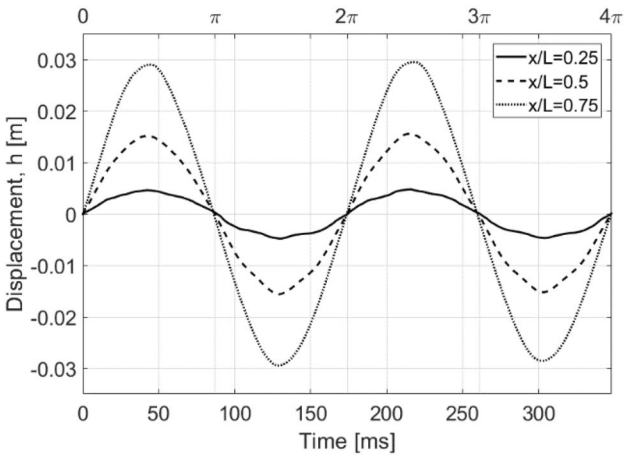

Fig. 11 Time evolution of foil displacement at x/L: 0.25, 0.5 and 0.75, at the mid-span location ($y/W = 0.5$)

The in-phase displacement, for all positions, indicates that the foil motion is dominated by its first mode of oscillation, and a stationary wave at the frequency $f_{\text{foil}} = 5.7\text{Hz}$ is observed. This frequency is very close to the first natural frequency (regardless damping) of the studied configuration, $f_{1,\text{natural}} = 5.17\text{Hz}$. This mode of oscillations is consistent with the theory of oscillating cantilevered beams (Den Hartog 1985), where the displacement increases more than linearly from root to tip.

6 Discussion on the closure of Collar's triangle

The time evolutions of all measured aeroelastic forces acting on tiles of 0.25 cm^2 area (0.5 cm × 0.5 cm) are presented in Fig. 12. The value of such forces is extracted at the three tile locations $x/L = \{0.25, 0.5, 0.75\}(y/W = 0.5)$. An observation can be made of the relative phase of the forces with respect to the motion of the foil. The tile's inertia force features a standing wave in-phase with the displacement h, which is consistent with the operator of second derivative between position and acceleration for an oscillatory signal. Therefore, the tile acceleration signal is in phase-opposition, (i.e. π phase-shift) to the displacement. Based on Eq. 2, the inertia (red line in Fig. 12) has opposite sign to the acceleration, leading to a condition of zero phase shift (in-phase signals) between displacement and inertia force. As expected from the measurement technique, the inertia force has the lowest uncertainty of the triangle, $\varepsilon_{inertia} = 6 \times 10^{-6}$ N.

The elastic force (in yellow, Fig. 12) should exhibit a value that is in phase opposition to the displacement and the inertia force. This behaviour is found back at $x/L = 0.75$ (Fig. 12-right). However, the variations in time do not feature a sinusoidal behaviour and the signal appears to be corrupted by spurious fluctuations at a frequency higher than that of the primary oscillation. At points closer to the root of the foil ($x/L = 0.25$ and $x/L = 0.75$), it appears that these spurious fluctuations compromise the evaluation of the elastic force as the noise level attains the same level of the expected magnitude of the elastic force. Overall, based on error propagation through the spatial regression onto the fourth derivative of the deformation, the elastic force presents the highest uncertainty $\varepsilon_{elastic} = 2 \times 10^{-4}$ N.

Finally, the aerodynamic force (shown in blue in Fig. 12) displays the lowest force levels among the three components and for the three locations of the foil. Differently to inertia and elastic forces, the aerodynamic force appears as a travelling wave with a different delay to the foil motion at each chord location. The latter can be also observed from the surface pressure in Fig. 9. This effect is explained by the streamwise convection of Kármán vortices featuring low-pressure blobs at their core. The uncertainty for the aerodynamic force resulted in $\varepsilon_{aero} = 4.3 \times 10^{-5}$ N.

The condition of maximum forcing for the aerodynamic force occurs when the aerodynamic force and the foil velocity are in phase. In such condition, the alignment between the aerodynamic force and the foil velocity vectors transfers

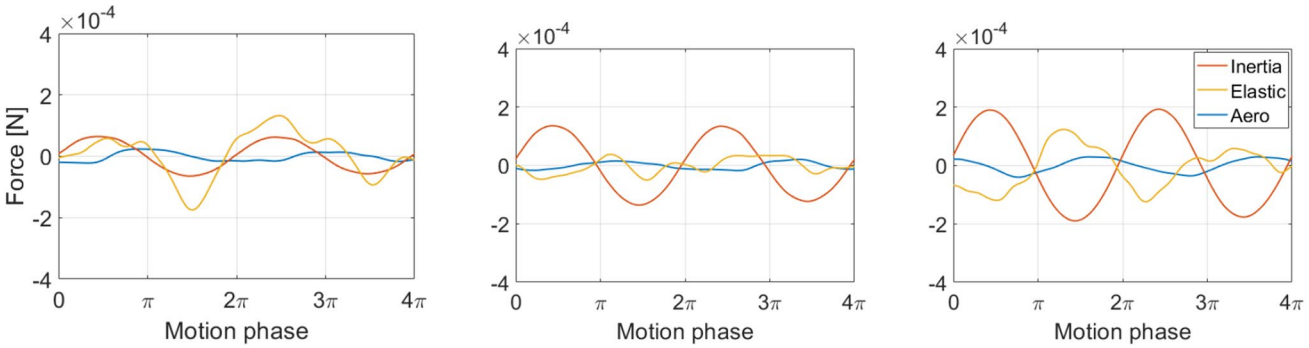

Fig. 12 Instantaneous time-evolution of aeroelastic forces at different chord locations x/L: 0.25 (left), 0.5 (centre), and 0.75 (right). Measurements at mid-span location $y/W = 0.5$

Table 3 Collar closure criterion force and inertia force for a tile location at $y/W = 0.5$

	$x/L = 0.25$	$x/L = 0.5$	$x/L = 0.75$
STD F_i (mN)	4.4×10^{-2}	9.4×10^{-2}	13.2×10^{-2}
STD ε_{CC} (mN)	11.2×10^{-2}	8.7×10^{-2}	6.2×10^{-2}
STD ε_{CC}/STD F_i	2.5	0.9	0.47

the maximum work from the flow to the foil. Therefore, the aerodynamic force must anticipate the foil's motion (displacement) by a phase shift of about $\pi/2$ (phase quadrature). From the present experiments (Fig. 12), it appears that such condition is best attained around the position $x/L = 0.75$.

Once the foil reaches a steady-state oscillatory regime (of approximately constant amplitude and frequency), only a small aerodynamic force is required to maintain the system in such regime, where the sum of elastic and inertia forces conserve most of the system kinetic energy. Instead, the work produced by the aerodynamic force is dissipated by structural damping. The evaluation of structural losses, however, goes beyond the scope of the current study and is not examined further.

The closure of Collar's triangle concludes this work and is achieved by imposing the equilibrium of the aeroelastic forces. The equilibrium addresses the dominant effects along the z-component of the force vector. When uncertainties pertaining to the experimental approach and the subsequent modelling to estimate the forces are accounted for by a term ε_{CC}, Eq. 1 is rewritten as:

$$F_i + F_e + F_a = \varepsilon_{CC} \tag{8}$$

This residual was anticipated in Sect. 2 as the Collar closure criterion (CC), ε_{CC}, and quantifies how accurate the measurement of three aeroelastic forces is altogether. For the present experiments, the closure of Collar's triangle (i.e. the magnitude of the residual force, ε_{CC}) is evaluated for the afore-analysed tile locations. In view of the oscillatory nature of the forces, the standard deviation (STD) of the error is reported in Table 3 taking the inertia force as a reference for the amplitude.

While the inertia force increases downstream, ε_{CC} increases towards the root. This is ascribed to the uncertainty of the elastic force, which appears to be maximum at the foil's root, with the small displacements. The ratio between the Collar force and the inertia force as provided in Table 3 can be seen as an indicator of the accuracy of the closure of Collar's triangle of forces. It is evident that from the foil's root to approximately the half chord ($x/L = 0.5$), the residual of Collar's force strongly distorts the equilibrium. As previously mentioned, this is ascribed to the large uncertainty of the elastic force associated with the fourth spatial derivative of displacements, and the vanishing magnitude of the inertia force close to the foil's root. Instead, towards the foil's tip ($x/L \geq 0.75$), the residual tends to become a vanishing component, indicating the feasibility of Collar's triangle closure by non-intrusive experimental means.

Aside from the uncertainty of the elastic force the hypothesis of small displacements will require further scrutiny. When the latter assumption is not satisfied, aerodynamic elastic and inertia forces will need to be evaluated with their full vectors and the local orientation of the foil needs to be accounted for.

7 Conclusions

A non-intrusive measurement methodology for aeroelastic experiments based on the Lagrangian particle tracking technique is proposed to simultaneously estimate aerodynamic, elastic and inertial loads from a deforming model. The method relies on the tracking of flow tracers to characterize the flow, and of surface markers to describe the dynamics of the structure. An experiment was carried out to show the applicability of the proposed methodology. The measurements regarded a flexible transparent foil attached to a solid cylinder and interacting with the wake of the latter. Both the flow tracers (neutrally-buoyant HFSB) and surface markers applied onto the panel were tracked in time with a single optical tomographic system.

The results show the potential of evaluating the aeroelastic forces from Lagrangian particle tracking measurements of the flow tracers and the markers on the flexible structure. The inertia forces were successfully evaluated via time-derivation of the markers' displacements. The pressure on the foil surface was obtained extrapolating the solution of the Poisson problem from the outer flow field to the foil. The elastic forces required evaluation of the fourth spatial derivative of the displacement and turned out to be the most challenging quantity to determine.

Flow analysis results show that pressure blobs associated with the Karman vortices determine the unsteady aerodynamic forcing. A phase shift exists between such external loading and the inertial and elastic response.

The Collar closure criterion is introduced that considers the residual of the force equilibrium equation as a measure of the accuracy of the overall experiment. The criterion yields unfavourable results close to the foil root where displacement and acceleration are vanishing. At the foil trailing edge, a consistent combination of the aeroelastic forces is observed, indicating the feasibility of the present optical diagnostic approach for aeroelastic systems characterisation.

Supplementary Information The online version contains supplementary material available at https://doi.org/10.1007/s00348-022-03468-9.

Acknowledgements The research leading to these results received funding from the project HOMER (Holistic Optical Metrology for Aero-Elastic Research), which is funded by the European Commission, programme H2020 under Grant No. 769237.

Declarations

Conflict of interest The authors state that there are no conflicts of interest related to this study.

References

Abdelkefi A (2016) Aeroelastic energy harvesting: a review. Int J Eng Sci 100:112–135

Adrian L, Adrian RJ, Westerweel J (2011) Particle image velocimetry. Cambridge University Press

Beresh S (2021) Time-resolved particle image velocimetry. Measurement Science and Technology

Bhattacharya S, Vlachos PP (2020) Volumetric particle tracking velocimetry (PTV) uncertainty quantification. Exp Fluids 61(9):1–18

Bleischwitz R, De Kat R, Ganapathisubramani B (2017) On the fluid-structure interaction of flexible membrane wings for MAVs in and out of ground-effect. J Fluids Struct 70:214–234

Boden F, Kirmse T, Poroikov AY, Rinkevichyus BS, Skornyakova NM, Shashkova IA (2014) Accuracy of measurement of dynamic surface deformations by the image pattern correlation technique. Optoelectron Instrum Data Process 50:474–481

Burner AW, Liu T (2001) Videogrammetric model deformation measurement technique. J Aircr 38:745–754

Chu TC, Ranson WF, Sutton MA (1985) Applications of digital-image-correlation techniques to experimental mechanics. Exp Mech 25:232–244

Collar AR (1946) The expanding domain of aeroelasticity. Aeronaut J 50:613–636

De Figueiredo HV, Castillo-Zúñiga DF, Costa NC, Saotome O, da Silva RGA (2020) Aeroelastic vibration measurement based on laser and computer vision technique. Experimental Techniques, 1–13

Den Hartog, JP (1985) Mechanical vibrations. Courier Corporation

De Kat R, Van Oudheusden BW (2012) Instantaneous planar pressure determination from PIV in turbulent flow. Exp Fluids 52(5):1089–1106

Elsinga GE, Scarano F, Wieneke B, van Oudheusden BW (2006) Tomographic particle image velocimetry. Exp Fluids 41(6):933–947

Friedmann PP (2004) Aeroelastic scaling for rotary-wing aircraft with applications. J Fluids Struct 19:635–650

Fung YC (2008) An introduction to the theory of aeroelasticity. Courier Dover Publications

Giovannetti LM, Banks J, Turnock SR, Boyd SW (2017) Uncertainty assessment of coupled digital image correlation and particle image velocimetry for fluid-structure interaction wind tunnel experiments. J Fluids Struct 68:125–140

Jeon YJ, Müller M, Michaelis D and Wieneke B (2018) Efficient reconstruction of flow field with pressure from particle tracks: VIC. Bull Am Phys Soc 63

Jux C, Sciacchitano A, Scarano F (2020) Flow pressure evaluation on generic surfaces by robotic volumetric PTV. Meas Sci Technol 31(10):104001

Kalmbach A, Breuer M (2013) Experimental PIV/V3V measurements of vortex-induced fluid–structure interaction in turbulent flow—A new benchmark FSI-PfS-2a. J Fluids Struct 42:369–387

Kehoe MW (1995) A historical overview of flight flutter testing

Liu X, Katz J (2006) Instantaneous pressure and material acceleration measurements using a four-exposure PIV system. Exp Fluids 41:227

Panc V (1975) Theories of elastic plates. Springer Science & Business Media

Peeters B, Hendricx W, Debille J, Climent H (2009) Modern solutions for ground vibration testing of large aircraft. Sound Vib 43(1):8

Percin M, Vanierschot M, Van Oudheusden BW (2017) Analysis of the pressure fields in a swirling annular jet flow. Exp Fluids 58:166

Marshall JG, Imregun M (1996) A review of aeroelasticity methods with emphasis on turbomachinery applications. J Fluids Struct 10:237–267

Mitrotta FM, Sciacchitano A, Sodja J, De R. and Breuker BW (2019) Experimental investigation of the fluid-structure interaction between a flexible plate and a periodic gust by means of Robotic Volumetric PIV. In Proceedings of the 13th international symposium on particle image velocimetry. Universitat der Bundeswehr Munchen.

Montgomery DC, Peck EA, Vining GG (2021) Introduction to linear regression analysis. Wiley

Neeteson NJ, Bhattacharya S, Rival DE, Michaelis D, Schanz D, Schröder A (2016) Pressure-field extraction from Lagrangian flow measurements: first experiences with 4D-PTV data. Exp Fluids 57:1–8

Sarkar PP, Jones NP, Scanlan RH (1994) Identification of aeroelastic parameters of flexible bridges. J Eng Mech 120:1718–1742

Scarano F, Ghaemi S, Caridi GCA, Bosbach J, Dierksheide U, Sciacchitano A (2015) On the use of helium-filled soap bubbles for large-scale tomographic PIV in wind tunnel experiments. Exp Fluids 56:42

Schanz D, Gesemann S, Schröder A (2016) Shake-The-Box: Lagrangian particle tracking at high particle image densities. Exp Fluids 57:70

Schanz D, Gesemann S, Schröder A, Wieneke B, Novara M (2012) Non-uniform optical transfer functions in particle imaging: calibration and application to tomographic reconstruction. Meas Sci Technol 24:024009

Schlichting H, Gersten K (2016) Boundary-layer theory. Springer

Schneiders JFG, Scarano F (2016) Dense velocity reconstruction from tomographic PTV with material derivatives. Exp Fluids 57:1–22. https://doi.org/10.1007/s00348-016-2225-6

Schuster DM, Liu DD, Huttsell LJ (2003) Computational aeroelasticity: success, progress, challenge. J Aircr 40:843–856

Sciacchitano A, Leclaire B, Schroeder A (2021) Main results of the first lagrangian particle tracking challenge. In: Proceedings of 14th

international symposium on particle image velocimetry 2021 (Vol. 1, No. 1, pp. 1–14). ILLINOIS Tech/Paul V. Galvin Library.
Soloff SM, Adrian RJ, Liu ZC (1997) Distortion compensation for generalized stereoscopic particle image velocimetry. Meas Sci Technol 8:1441
Timpe A, Zhang Z, Hubner J, Ukeiley L (2013) Passive flow control by membrane wings for aerodynamic benefit. Exp Fluids 54:1471
Van Oudheusden BW (2013) PIV-based pressure measurement. Meas Sci Technol 24:032001
Wan Z, Cesnik CE (2014) Geometrically nonlinear aeroelastic scaling for very flexible aircraft. AIAA J 52:2251–2260
Wieneke B (2008) Volume self-calibration for 3D particle image velocimetry. Exp Fluids 45(4):549–556
Williamson CH (1996) Vortex dynamics in the cylinder wake. Annu Rev Fluid Mech 28(1):477–539
Wright JR, Cooper JE (2008) Introduction to aircraft aeroelasticity and loads. Wiley

Authors and Affiliations

Gabriel González Saiz[1] · Andrea Sciacchitano[1] · Fulvio Scarano[1]

✉ Gabriel González Saiz
G.GonzalezSaiz@tudelft.nl

[1] Faculty of Aerospace Engineering, Delft University of Technology, Delft, The Netherlands